



Optimized pixel level image fusion for lung cancer detection over MRI and pet image

Lekshmi V. Nair¹ · S. Albert Jerome¹

Received: 28 February 2023 / Revised: 27 December 2023 / Accepted: 22 March 2024 /

Published online: 15 April 2024

© The Author(s), under exclusive licence to Springer Science+Business Media, LLC, part of Springer Nature 2024

Abstract

Lung cancer is an abnormal development of cells that are uncontrollably proliferating. When using a system for medical diagnostics, the precise identification of lung cancer is crucial. Magnetic Resonance Imaging (MRI) and Positron Emission Tomography (PET) are the most common methods for diagnoses. Due to the limited sensitivity of the border pixels in PET and MRI imaging, finding lung cancer might be difficult. As a result, image fusion was created, which successfully combines several modalities to identify the disease and cure it. But merging images from multiple modalities has always been troublesome in medicine because the final image includes distorted spectral information. To avoid the problems, in this paper, pixel level image fusion for lung cancer detection is proposed. Pre-processing, multi-modality image fusion, feature extraction, and classification are the four phases of the suggested methodology. Images from the PET and MRI scanners are initially gathered and pre-processed. The best pixel-level fusion method is then used to merge the PET and MRI images. Here, the adaptive tee seed optimization (ATSO) method is used to ideally choose the fusion parameter contained in the approach to improve the fusion model. The texture characteristics are taken from the fused image after the image fusion. The deep extreme learning machine (DELM) classifier will then identify an image as normal or abnormal using the retrieved features. Utilizing a variety of criteria, the effectiveness of the suggested methodology is assessed and compared to previous state-of-art studies. The experimental results shows proposed approach attained the maximum accuracy of 97.23%.

Keywords Magnetic reasoning imaging · Positron Emission Tomography · Image fusion · Lung cancer · Adaptive tee seed optimization · And deep extreme learning machine

✉ Lekshmi V. Nair
lekshmilive@gmail.com

¹ Department of Biomedical Engineering, Noorul Islam Centre for Higher Education, Kumaracoil, Kanyakumari District, Thuckalay, Tamil Nadu, India

1 Introduction

The word "lung carcinoma" is frequently used to refer to lung cancer, which is a malicious lung tumor characterized by unchecked cell growth in the lung tissues that eventually results in death. Therefore, it's critical to get an earlier-stage lung cancer diagnosis [1, 2]. When there are any harmful or anomalous conditions existing in the lungs, the MRI or PET images provide details regarding the lungs [3, 4]. However, there are situations when the visuals needed for diagnosis aren't easily recognizable or understandable to the human eye. Therefore, image fusion techniques were used for the MRI and PET images for easy viewing.

Fusing two or more images creates an image that combines the information within each source image. Pixel-level fusion, feature-level fusion, and decision-level fusion are the three tiers of image fusion methods [5]. A direct fusion approach is fusion at the pixel level. The mixing of color information from the human eye is an illustration of pixel-level fusion. It merges all gathered data at the pixel level. In image fusion, the pixel level is the lowest [6]. Due to its great precision, this level of data fusion can give information that is not present at lower levels. Pixel points must be rigorously registered to maintain more original image data and to provide rich, precise, and trustworthy information. As a result, it is beneficial for additional image analysis, processing, and comprehension. It is easier for humans to understand an image that has been concatenated at the pixel level. This benefit has made medical imaging more effective at detecting cancer cells inside organs.

The use of medical images improves understanding of medical problems [7]. Fusion produces higher pixel changes in focused regions. In pixel-based techniques, pixels can be picked incorrectly because of noise. Noise and distortion must be removed from the input images. Next, Adaptive Tree Seed Optimization (ATSO) is used to select the optimal pixels [8]. The MRI/PET image classification has been approached using many different methods, including decision trees, Bayes classifiers, local backpropagation algorithms, Support Vector Machines (SVMs), Batch Incremental Support Vector Machines (BISVMs), K-nearest neighbors, and Extreme Learning Machines (ELM). However, deep learning algorithms do not have such limitations, as most shallow neural network algorithms approximate complex functions that are subject to some restrictions.

So the Deep Extreme Learning Machine (DELM) method is introduced in this study. A deep learning algorithm uses multilayer perceptions in artificial neural networks. Approximating complex functions with deep learning has reduced optimization challenges associated with deep models. Single-layer feed-forward neural networks (SLFNs), created by Huang et al., are employed in ELM. By combining deep learning and extreme learning machines, DELM can achieve great results. MRI/PET images were also classified as normal or pathological using the DELM classifier [9]. DELM uses a single-hidden layer neural network for image classification. In DELM, speed and other characteristics can improve learning accuracy. Automatic idea selection and adaptive activation enhance classification. For image classification, DELM has a high degree of generalization accuracy. DELM is more accurate than traditional methods of classifying lung MRI/PET images.

The main aim of the proposed methodology is to automatically detect lung cancer from the multi-modal fused image. For multi-modal fusion, PET and MRI images are used. For better image representation and classification, we apply the fusion process. For classification, we fused the MRI and PET image based on the fusion rule. Then,

from the fused image, we extract the texture features. The DELM classifier is then instructed to categorize animage as normal or abnormal using the retrieved characteristics. The following is a list of the suggested approach's significant contributions:

- From all the source images, a segmentation map is produced using the region-growing segmentation method.
- The source images are divided into various orientations and scales using the 3L-DWT.
- The segmentation map and the pixel-based decision maps are used to create the region-dependent decision maps.
- Fuzzy logic is used to combine the outcomes of three distinct fusion guidelines relying on the dissimilarity metric of the input image: selection using a pixel-based decision map, selection using a region-dependent decision map, and weighted averaging. This results in the high-frequency wavelet coefficients of the input image.
- The weights are optimally calculated using the adaptive tree seed optimization (ATSO) approach and weighted averaging is employed to obtain the low-frequency wavelet coefficients of the final fused image.
- The inverse 3L-DWT of the new low and high-frequency wavelet coefficients results in the final fused image.
- Texture features are taken from the fused image.
- The DELM classifier uses the retrieved characteristics to determine whether animage is benign or cancerous.
- Various measures are used to analyze the performance of the suggested technique.

The rest of the paper is organized as follows; the literature survey of the proposed topic is explained in Section 2 and the proposed methodology concept is deeply explained in Section 3. The experimental results are discussed in Section 4 and the conclusion part is presented in Section 5.

2 Literature survey

Deep learning algorithms for lung cancer diagnosis were given by Asuntha and Srinivasan A. [10]. It employs methods for extracting features including the Histogram of Oriented Gradients (HoG), Local Binary Pattern (LBP), wavelet transform-based features, Zernike Moment, and Scale Invariant Feature Transform (SIFT). After gathering textural, geometry, volumetric, and intensity data, the best feature was selected using the Fuzzy Particle Swarm Optimization (FPSO) method. Then the classification was done using CNN. This increases speed and lowers high calculation costs. This technique's categorization performance has to be enhanced.

The DGMM-RBCNN framework, developed by Jena and Ponraj [11] was an effective lung carcinoma diagnostic tool. Using DGMM and CNN classifier, a region-growing segmentation algorithm was employed to successfully diagnose lung carcinoma. Here, a successful segmentation was applied to divide the ROI. All of the procedures used at different levels were straightforward to put into practice. This demonstrates that processing a large volume of data in an iteration period was highly quick and effective. There was an accuracy of 87.79% for the DGMMclassification RBCNN, although it might need to be increased.

Convolutional neural networks (CNN) and feature-based methodologies for lung cancer diagnosis were presented by Guo et al. [12]. The enhanced Harris hawk optimizer was used in

the first stage to optimize the CNN classifier. The dataset was subjected to this methodology, and classification is started. The findings are sent to the second classifier the feature-based approach—if this technique was unable to detect the illness. The dataset that was acquired from the CNN classifier was further applied to this classifier, which includes characteristics from Haralick and LBP. Ultimately, it was considered safe if the feature-based technique also doesn't detect cancer; if it does, it is malignant. Classification accuracy is good, reaching 97%. The length of this method's computation was high.

The fuzzy-based segmentation algorithm was introduced by Akter et al. [13]. The lung scan images are characterized by their highest and lowest values together with the row and column values respectively; this method automatically selects its starting cluster value. To enhance segmentation accuracy, the algorithm continues the process. Structure and texture properties were retrieved using the gray-level co-occurrence matrix. Next, the lung nodule was classified as harmless or carcinogenic using a neuro-fuzzy classifier. With a 90% accuracy rate, the suggested approach could automatically identify early-stage lung cancer. Parvathy and Pothiraj [14] developed a model for the efficient clinical image fusion approach that uses the Binary Crow Search Optimization (BCSO) algorithm and discrete wavelet transform. To enhance the quality of the image, the noise included in the source photos was first eliminated using a median filter. The fusion process was performed after applying a discrete wavelet transform to both input modalities. The info from the two image models was then combined via the fusion algorithm. The fusion rule parameters are selected optimally using the Binary Crow Search Optimization (BCSO) method. This method yields outstanding results with 6.63 entropy, 0.849 SSIM, and 5.9 FF. The accuracy of these methods has to be improved nevertheless.

The non-sub-sampled contourlet transform (NSCT) and CNN-based multimodal fusing of clinical images approach was first introduced by Wang, et al. [15]. To get superior fusing outcomes, this approach makes use of both NSCT and CNN benefits. Input multi-modality images were divided into low and high-frequency sub-bands using this approach. Like an adaptable fusing rule for high-frequency sub-bands, a brand-new Perceptual High-Frequency CNN (PHF-CNN) that has been trained in the frequency domain was developed. The decision map for the low-frequency sub-band was made using two result maps. Lastly, the inverse NSCT was utilized to merge fused frequency sub-bands. For the greyscale images, this approach performed well overall. It is unable to merge color images.

Fu et al. [16] developed the deep Convolutional Neural Network-dependent multimodal biomedical image fusion algorithm and the rolling guiding filter. The VGG network was used to enhance the edges and features of the image. Initially, the base and details of the images were extracted using the rolling guidance filter. To enhance the fusion efficiency, the VGG network also gathered the perceptual images. Lastly, three distinct fusion algorithms were employed to combine the base, detail, and perceptual images. Also, the normalization process was employed to remove noise and feature discrepancies from the perceptual images that the VGG network had generated. This technique reduces the fusion processing time, but the noise in the images degrades the outcome quality and distorts the colors.

3 Proposed lung cancer detection methodology

The principal purpose of this study is to accurately identify lung cancer on lung patient imaging. We use the fusion approach for more precise detection. Here, we combine images from two different imaging modalities, namely MRI and PET. The ATSO method is used

to create the fusion. Figure 1 shows the general layout of the unique image fusion-based lung cancer classification approach.

3.1 Fusion of multi-modal image

We outline the suggested fusing of the multi-modal image strategy in this section. Figure 2 depicts the general structure of multi-modal fusion, and the next section explains each stage in deta.

3.1.1 Image segmentation

This section intends to use a region-growing algorithm to segment the original image. We determine the joint gradient magnitude of the source images before segmentation to improve the segmentation result. The source image S_{in} contains MRI images I_M and PET image I_P . Following is an explanation of the joint gradient magnitude step;

The joint gradient (JG) is initially computed to use the function of the Gaussian derivative $G(i, j)$, to construct the magnitude of the gradient from the source image S_{in} .

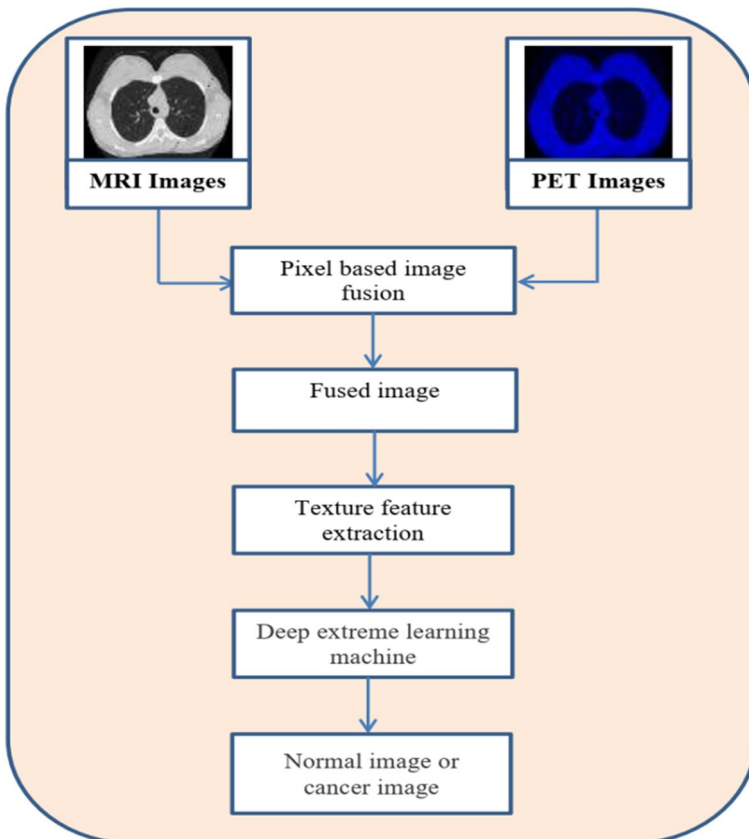


Fig. 1 The basic layout of the presented technique

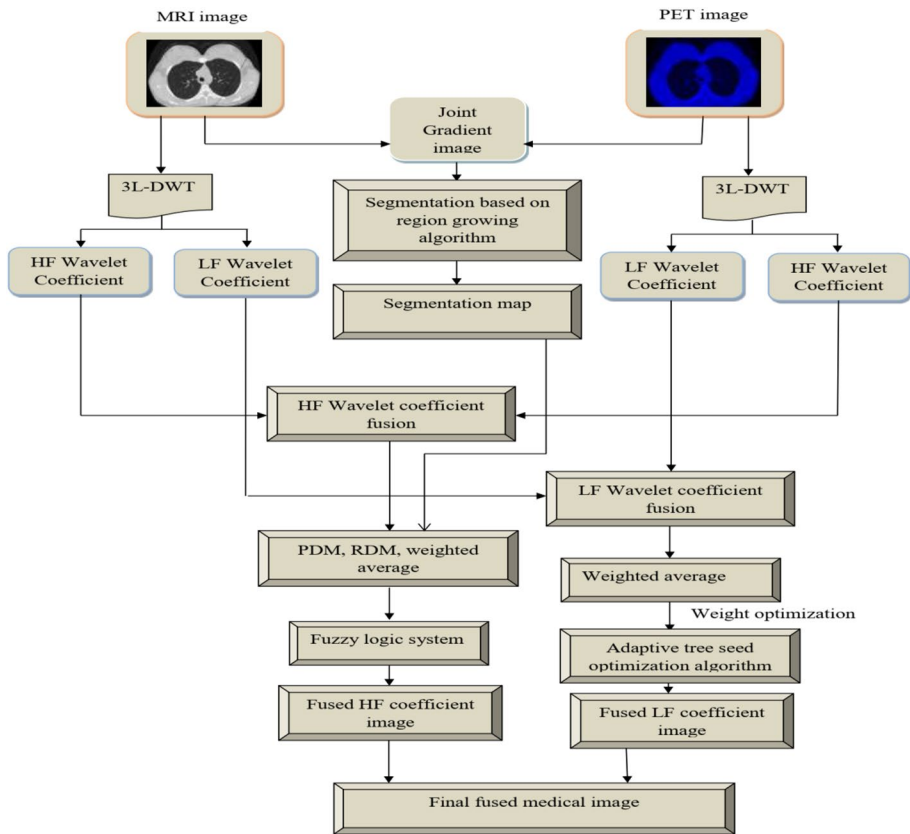


Fig. 2 Proposed fusion process

$$G_{S_m}(i,j) = \sqrt{(S_{in}(i,j) * G'_i)^2 + (S_{in}(i,j) * G'_j)^2} \quad (1)$$

In this case, a grayscale image is shown as $S_{in}(i,j)$, Filters with Gaussian partial derivatives are used to represent G'_i and G'_j in i and j directions and $*$ is represented as convolution.

- Following $G(i,j)$ the assessment, we get the image's JG using an Eq. (1). Equation (2) contains the JG computation.

$$JG(i,j) = \frac{1}{2} \left(\frac{\tilde{G}_{I_M}(i,j)}{\max_{ij} \tilde{G}_{I_M}(i,j)} + \frac{\tilde{G}_{I_P}(i,j)}{\max_{ij} \tilde{G}_{I_P}(i,j)} \right) \quad (2)$$

where; G_{I_M} is an MRI image with a filtered gradient and G_{I_P} stands for the PET's filtered gradient image.

- Following the calculation of the image's joint gradient, we use the region-growing segmentation to produce the segmentation map S_M .

3.1.2 Discrete wavelet transform-based image decomposition

We use the discrete wavelet transform to deconstruct the image after creating the segmentation map. We employ the three-level discrete wavelet transform for decomposition (3L-DWT). We acquired the four sub-bands LL, LH, HH, and HL during the first level of decomposition, where LL stands for the approximation coefficients. The detailed coefficients are represented by the letters LH, HL, and HH. The vertical, horizontal, and diagonal coefficients are denoted by the first, second, and third components of detailed coefficients, respectively. The second level of decomposition then uses the previous level's approximation band (LL) as input and generates four more sub-band images. The third level of decomposition yields an additional four sub-bands in the image. Figure 3 shows the 3-level image decomposition's organizational structure.

The coefficients at the sub-bands are determined at the initial level of wavelet decomposition using the formulae below;

LL band

$$a_{i+1}(n_1, n_2) = \sum_{k_1=0}^{L-1} \sum_{k_2=0}^{L-1} H_0(k_1) H_0(k_2) S_M(2n_1 - k_1, 2n_2 - k_2) \quad (3)$$

LH band

$$d_{i+1}(n_1, n_2) = \sum_{k_1=0}^{L-1} \sum_{k_2=0}^{L-1} H_0(k_1) H_1(k_2) S_M(2n_1 - k_1, 2n_2 - k_2) \quad (4)$$

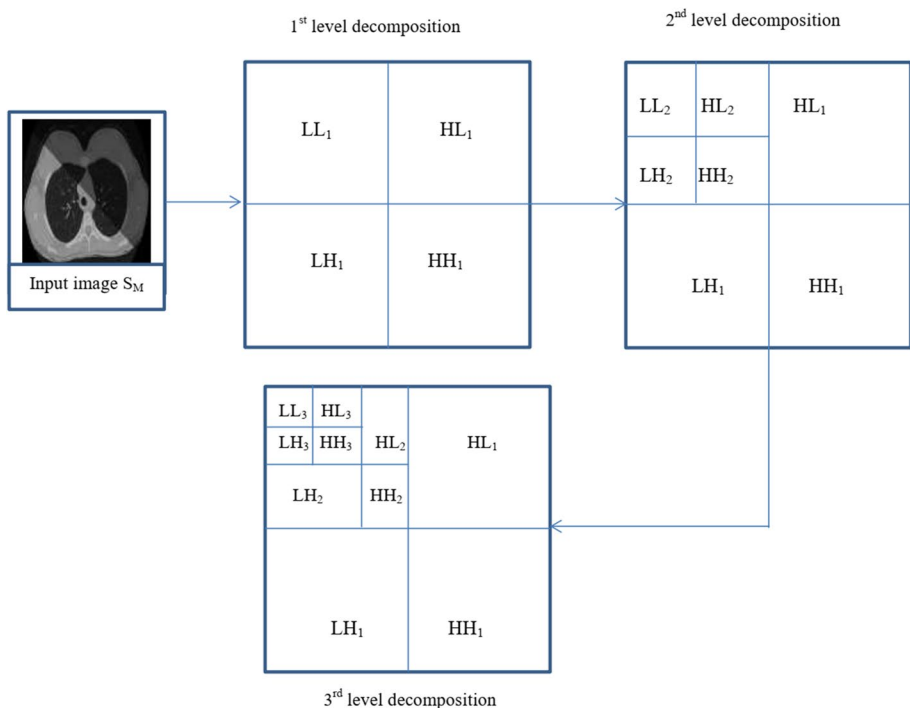


Fig. 3 Schematic structure of 3-level wavelet image decomposition

HL band

$$d_{i+1}(n_1, n_2) = \sum_{k_1=0}^{L-1} \sum_{k_2=0}^{L-1} H_1(k_1) H_0(k_2) S_M(2n_1 - k_1, 2n_2 - k_2) \quad (5)$$

HH band

$$d_{i+1}(n_1, n_2) = \sum_{k_1=0}^{L-1} \sum_{k_2=0}^{L-1} H_1(k_1) H_1(k_2) S_M(2n_1 - k_1, 2n_2 - k_2) \quad (6)$$

where, k_1 and k_2 indicate the image's columns and rows and L represent the filter size. The other bands are calculated using Eqs. (3–6). Then, for subsequent processing, the low-frequency and high-frequency bands are employed.

3.1.3 Decision map creation

Since we apply the wavelet-based image fusion technique to diagnose lung cancer in this work, this section calculates the pixel and region-based decision map. In general, the visual system of humans is sensitive to contrast changes or edges, which makes wavelet image fusion methods challenging. Using this information, the MRI image's area borders and the PET image's information are combined using the wavelet transform domain (texture of areas). MRI and PET images are transformed using wavelet transform coefficients, and the Decision Map (DM) determines the most significant coefficients.

- Pixel-dependent decision map (PDM) generation

The quality of a particular region of each source image is evaluated using the activity level assessment in the transformation domain. The local standard deviation is obtained by multiplying the magnitude of the complex wavelet coefficients of the source images, and in this case, it is employed as a window-dependent function.

$$P_{abs}^m(\cdot|d) = \sqrt{P_{real}^m(\cdot|d)^2 + P_{imag}^m(\cdot|d)^2} \quad (7)$$

$$F^m(i, j|d) = \sqrt{\frac{1}{W} \sum_{n=-N}^N \sum_{m=-M}^M \left(\left| P_{abs}^m(i+n, j+m|d) \right| - \left| P_{abs}^{-m}(\cdot|d) \right| \right)} \quad (8)$$

where;

$P_{imag}^m(\cdot d)$	HF wavelet coefficient in the imagination.
$P_{real}^m(\cdot d)$	Coefficient of wavelet for real high frequency.
m	Level of decomposition.
d	High-frequency wavelet coefficients' direction ($\pm 15^\circ$, $\pm 45^\circ$ and $\pm 75^\circ$).
d	1, 2... 6.
W	Local window Pixel count $[2N + 1, 2M + 1]$.
(\cdot)	Spatial location is indicated in shorthand.

To account for neighbor dependency, the local features are retrieved from the complex wavelet coefficient's magnitude, and the feature space is smoothed by a nonlinear average in the local window:

$$NF^m(i, j | d) = \sum_{n=-N}^N \sum_{m=-M}^M L(n, m) \times F^1(i + n, j + m | d) \quad (9)$$

here;

F Local feature.

$L(n, m)$ The weight of the local window, as determined by the Gaussian filter.

Equation (10) is used to generate the PDM for each level of decomposition and direction:

$$PDM^m(\cdot | d) = \begin{cases} 1 & \text{if } NH_{K_M}^m(\cdot | d) > NH_{K_C}^m(\cdot | d) \\ 0 & \text{Otherwise} \end{cases} \quad (10)$$

where;

$NH_{K_M}^m(\cdot | d)$ and $NH_{K_C}^m(\cdot | d)$ features extracted from input source image using (9),

m The level of decomposition.

d $d = 1, 2, \dots, 6$ is the direction of HF coefficient for wavelet ($\pm 15^\circ$, $\pm 45^\circ$ and $\pm 75^\circ$)

(\cdot) Spatial position indicated in shorthand.

- Region-dependent decision map (RDM) formation

The decision map for picking more relevant HF coefficients between the sources images can also be made using RDM, however, this method is unreliable and highly susceptible to the huge coefficients in the area [17]. Therefore, we use a novel technique to generate the region-based decision map (RDM). As stated in Section 3.1.1, a composite segmentation map depending on all source images is first created. If the numbers in the PDM's corresponding area are larger than zero, the RDM's corresponding region is set to one by glancing at the named region; otherwise, it is set to zero. The following equation explains this:

$$RDM^m(P | d) = \begin{cases} 1 & \text{if } \left(\sum_{n \in R} PDM^m(n | d) \right) > \frac{|P|}{2} \\ 0 & \text{Otherwise} \end{cases} \quad (11)$$

where;

P Region with size $|R|$

PDM pixel-based decision map using (17).

m Decomposition level, and $d = 1, 2, \dots, 6$.

3.1.4 Fusion rule generation

Low and high-frequency wavelet coefficients are utilized to produce the fusion rules. The fusion process is governed by the rules.

A. Low-frequency wavelet coefficient-based rule

Since the LF coefficients transport the majority of an image's energy, the information in these coefficients is crucial to the natural appearance of an image. In most frequency-based approaches, averaging is a common technique for integrating the LF sub-bands of source images:

$$s_F^M(i, j) = \frac{s_{K_M}^M(i, j) + s_{K_C}^M(i, j)}{2} \quad (12)$$

where;

$s_F^M(i, j)$ Wavelet coefficient of fused LF.
 $s_{K_M}^M(i, j), s_{K_C}^M(i, j)$ Input wavelet coefficients of LF.
 M Level of coarsest resolution.

An LF fusion guideline that arithmetically merges the input coefficients of LF was developed by Petrovic and Xydeas [18]. Following is a description of the offset zero-mean addition:

$$s_F^M(i, j) = s_{K_M}^M(i, j) + s_{K_C}^M(i, j) - \frac{\mu_A + \mu_B}{2} \quad (13)$$

where; μ_A indicate the LF sub-band image's mean value (I_m) and μ_B represent the mean value of the LF sub-band image (I_p).

An alternate method of integrating the LF sub-bands of source images is the weighted average.

$$s_H^M(i, j) = \frac{W_{K_M}^M(i, j) \times s_{K_C}^M(i, j) + W_{K_C}^M(i, j) \times s_{K_M}^M(i, j)}{W_{K_M}^M(i, j) + W_{K_C}^M(i, j)} \quad (14)$$

where;

$s_H^M(i, j)$ Fused image.
 $s_{K_M}^M(i, j)$ and $s_{K_C}^M(i, j)$ Inputted wavelet coefficients of LF.
 L Level of coarsest resolution.

In this paper, we suggest a new weighted average approach, where the weights are computed by an optimization technique, for the fusing of the wavelet coefficients of LF.

$$s_H^M(i, j) = W_1(i, j) \times s_{K_C}^M(i, j) + W_2(i, j) \times s_{K_M}^M(i, j) \quad (15)$$

Here;

$t_H^M(i, j)$ Fused image.
 $t_{K_M}^M(i, j)$ and $t_{K_C}^M(i, j)$ Inputted wavelet coefficients of LF.

W1 and W2 are weight values between 0 and 1, and $W1 + W2 = 1$. The best weights to add to the final fused image's entropy index are determined via an optimization process.

B. Weight optimization using adaptive tree seed optimization (ATSO)

In this section, the weight values used in Eq. (12) have been carefully chosen. The ATSO method for weight optimization is provided. To enhance the infoon the wavelet coefficient of the LF fusion image, the weight values are tuned here. A population-based heuristic searching method called the suggested ATSO algorithm is put forth to address continuous optimization issues [8]. The TSO method is paired with the oppositional-based learning (OBL) technique to improve the performance of tree seed optimization. This OBL method is used to speed up execution while improving searchability. The following describes the steps involved in weight optimization;

Step 1: Solution encoding: In the solution encoding phase of the CBGA method, which represents weight sets (W1 and W2) initially. A solution is expressed vector with SL_k dimensions, where each dimension (position) is represented by a weight. The weight distribution information is highlighted in a solution SL_k (for the wavelet of LF coefficient fusion). k is between 1 and z , this shows the population's number of solutions. A solution SL_k consists of $w[i]$ and $w[j]$, this highlights the source image LF coefficient weighting information. When the maximum number of iterations is reached, the search is over. The format for the solution representation is shown in Fig. 4.

Step 2: Calculating the fitness: The fitness of every solution is determined following initialize of the solution. Fitness is defined as the entropy value. The entropy metric calculates the data content of animage for each solution. Entropy will be high in animage with large data content. Equation (16) is used to compute the entropy.

$$Entropy = \sum_{i=0}^K N(i) \times \log_2 (N(i)) \quad (16)$$

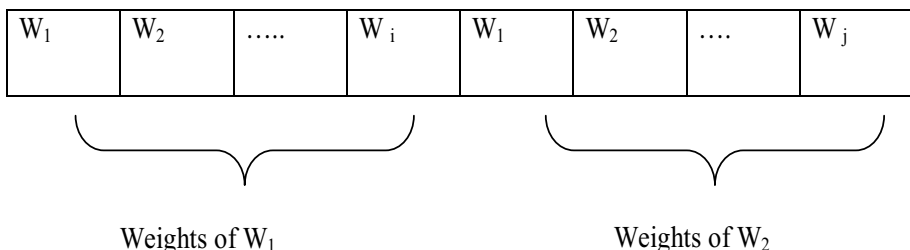


Fig. 4 A single solution representation format

where; the count of grey levels in the image is K , and N is the normalized histogram of the restored or fused image.

Step 3: Updating TSOA: After evaluating fitness, the TSO algorithm is used to update the solutions. The ST value affects how the TSO updates its position. The seed value is changed using (17) when the ST value is less than R_{ij} .

$$P_{ij} = T_{ij} + \alpha_{ij}(B_j - T_{r,j}) \quad (17)$$

Or else, the preceding equation is used to update the seed value;

$$P_{ij} = T_{ij} + \alpha_{ij}(T_{ij} - T_{r,j}) \quad (18)$$

Step 4: Operation of crossover: After the TSO update, the solutions are once again modified by employing the crossover operation. Through the crossover process, a new set of solutions is created from the previous ones. In Fig. 5, the cross-over operation is shown.

Step 5: Operation of mutation: The crossover is followed by mutation. The variability of each chromosome displayed in the image is maintained via mutations, which are the development of new children from single parents. The genotype of a kid might be altered arbitrarily. The performance of this gene is superior to that of elderly parents. Alternate and random mutations are the two types of mutation.

Step 6: Termination criteria: While choosing the best value for fitness is succeeded, the algorithm comes to an end. The resource distribution is handled after reaching the ideal level of fitness. In Fig. 6, the ATSOA flowchart is displayed.

C. High-frequency wavelet coefficients fusion rule

We find two different forms of decision maps, including pixel- and region-dependent decision maps, in section From source images, we choose the crucial coefficient of high-frequency wavelet for mapping.

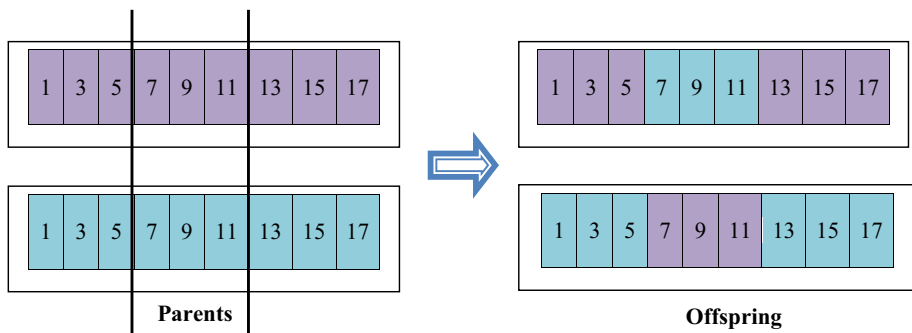


Fig. 5 Operation of crossover

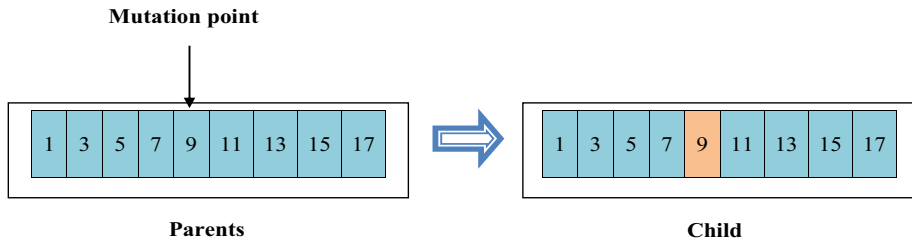


Fig. 6 Operation of mutation

- The following Eq. (19) is employed if coefficients of high-frequency wavelets are selected from the source images S_{in} using PDM. It will be impacted by issues like noise and imagemisregistration, and it typically produces artifacts in the fused image.

$$t_1^m(\cdot|d) = PDM^m(\cdot|d) \times t_{K_M}^m(\cdot|d) + (1 - PDM^m(\cdot|d)) \times t_{K_C}(\cdot|d) \quad (19)$$

- The following Eq. (20) is utilized if the coefficient of high-frequency wavelet is obtained from the source images S_{in} using RDM.

$$t_2^m(\cdot|d) = RDM^m(\cdot|d) \times t_{K_M}^m(\cdot|d) + (1 - RDM^m(\cdot|d)) \times t_{K_C}(\cdot|d) \quad (20)$$

where;

t_{K_M} and t_{K_C}	Source images' high-frequency wavelet coefficient.
m	Decomposition level.
(\cdot)	Spatial position notation using shorthand.
PDM	A decision map with pixels that is created using (17).
RDM	A region-based decision map that is created by (18).

Among the source images, there are some regions in which we have difficulty selecting the most important wavelet coefficients because the extracted features are not sufficiently different. To account for these pixels, we propose the following weighted average rule:

$$t_3^m(\cdot|d) = \frac{NH_{K_M}^m(\cdot|d) \times t_{K_M}^m(\cdot|d) + NH_{K_C}^m(\cdot|d) \times t_{K_C}^m(\cdot|d)}{NH_{K_M}^m(\cdot|d) + NH_{K_C}^m(\cdot|d)} \quad (21)$$

Here;

t_{K_M} and t_{K_C}	Source images' HF wavelet coefficient.
m	Decomposition level.
(\cdot)	Spatial position notation using shorthand.
$NH_{K_M}^m$ and $NH_{K_C}^m$	Extracted features utilizing (8) for input source images K_M and K_C .

D. Fuzzy logic-dependent rule selection for fusion

Three different forms of fusion rules are shown here, including weighted average (WA) dependent rules, region decision map (RDM) based rules, and pixel decision map (PDM)

based rules. The three fusion rules presented in (11)–(13) together fail to yield a useful fusion image. As a result, we combine three fusion rules to create a successful fusion approach using fuzzy logic.

A dissimilarity measure (DIS) of source images is established with this goal in mind. The DIS aims to express how "different" the source images are from one another.

$$DNH^m(i, j|d) = \left| NH_{K_M}^m(i, j|d) - NH_{K_C}^m(i, j|d) \right| \quad (22)$$

$$DIS^m(i, j|d) = \sqrt{\sin \left(\frac{\Pi \times DNH^m(i, j|d)}{2 \times T} \right)} \quad (23)$$

where;

First, relying on our findings, we formulate the preceding language rules for the fusion process:

-
- | | |
|--------|---|
| Rule 1 | At the given position IF the measure of DIS (i, j) is high (H), THEN the first fusion rule (1) (selection via PDM) is utilized |
| Rule 2 | At the given position IF the measure of DIS (i, j) is medium (M), THEN second fusion rule (2) (selection via RDM) is utilized |
| Rule 3 | At the given position IF the measure of DIS (i, j) is low (L), THEN third fusion rule (3) (weighted averaging (WA)) is utilized |
-

The fusion guidelines for integrating coefficients of high-frequency wavelet from the source images are described in the preceding formulation.:

$$t_H^m(\cdot|d) = \sum_{i=1}^3 t_i^m(\cdot|d) \times \mu_i(DIS^m(\cdot|d)) \quad (24)$$

where; $t_1^m(\cdot|d)$, $t_2^m(\cdot|d)$ and $t_3^m(\cdot|d)$ obtained using (11)–(13). μ_1 , μ_2 and μ_3 are the large medium and small membership functions respectively, l is decomposition level, $d = 1, 2, \dots, 6$ is the high-frequency wavelet coefficient's direction ($\pm 15^\circ$, $\pm 45^\circ$ and $\pm 75^\circ$), and (\cdot) is spatial position indication in shorthand.

3.1.5 Fusion of Source image

The primary research objective is to merge wavelet-dependent MRI and PET images. Here, we integrated the coefficients of HF and LF wavelet of source images in the aforementioned block. The fused HF wavelet coefficient and LF wavelet coefficient are combined in this block. Finally, using the wavelet coefficient, we discovered the combined source image. The equation produces the final fused image (25).

$$S_F = \psi^{-1} \left(s_H^M, t_H \right) \quad (25)$$

where;

- ψ Inverse 3L-DWT.
- t_H HF wavelet coefficient.
- s_H^M LF wavelet coefficient.

The fused image can be utilized for additional categorization procedures.

3.2 Feature extraction

We extract the GLCM texture characteristics from the input image after image fusion. The attributes that were retrieved are Contrast, Angular Second Moment, Inverse Difference Moment, Correlation, Entropy, Sum Variance, Variance, Sum Average, Difference Entropy, Sum Entropy, Inertia, Dissimilarity, Cluster Shade, Energy, Cluster Prominence, Homogeneity, and Variance. The information measure of correlation 1 and 2, and inverse difference normalized (INN) can be used to assess autocorrelation, maximum likelihood, and information measure of correlation, respectively.

3.3 Deep extreme learning machine (DELM)

Following feature extraction, the proposed classifier is provided with the extracted characteristics to categorize the data as normal or abnormal. To integrate the advantages of deep learning and ELM in the suggested study, we used the DELM. The DELM configuration design is depicted in Fig. 7 and consists of the layer of input having 22 neurons, six hidden layers having 10 neurons each, and the layer of output having 1 neuron. Both the input neuron sizes and the derived characteristics are inactive.

Equation (26) gives the first layer's input for the mathematical DELM, while Eq. (27) displays its output.

$$\alpha_i = s_1 + \sum_{j=1}^n (\beta_{ij} * z_j)$$

$$\gamma_i = \frac{1}{1+e^{-\alpha_i}}$$
(26)

where

$$i = 1, 2, 3, \dots, z$$
(27)

The second layer's feedforward propagation to the output layer in Eq is shown below (28).

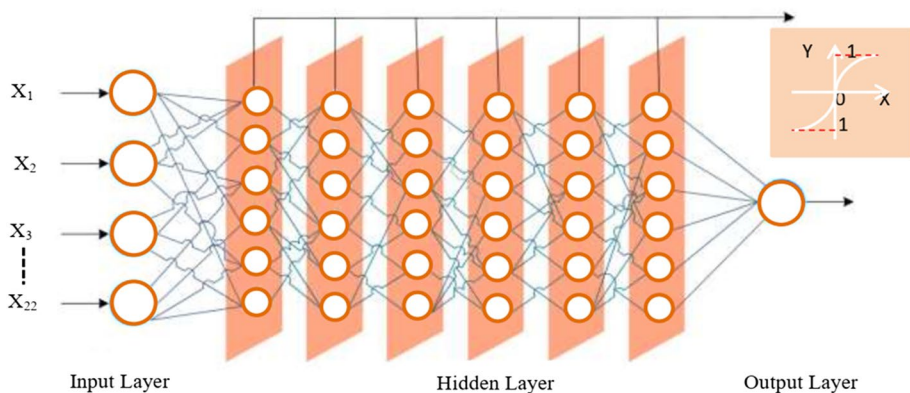


Fig. 7 Structural diagram of the proposed deep extreme learning machine (DELM)

$$\alpha_{1k} = s^k + \sum_{i=1}^m (x_{i1k=1} * \gamma_i^{k=1}) \quad (28)$$

Equation (29) shows the activation function of the output layer.

$$\gamma_{1k} = \frac{1}{1 + e^{-\alpha_{1k}^{k-1}}} \quad (29)$$

$$\alpha_{1k}^l = s^k + \sum_{i=1}^m (x_{il^k} * \gamma_i^k) \quad (30)$$

where, $k = 1, 2, 3 \dots 6$.

The following Eq. (31) represents the inaccuracy in propagation:

$$\xi = \frac{1}{2} \sum_1 (T \arg et_1 - \gamma_1^{k=6})^2 \quad (31)$$

where, $T \arg et_1$ and $\gamma_1^{k=6}$ indicate the intended and computed results respectively. The weight shift rate specified for the output layer is shown in Eq. (32).

$$\Delta \beta = \frac{\partial \xi}{\partial \beta} \quad (32)$$

$$\Delta \gamma_{i,1}^{k=6} = -\epsilon \frac{\partial \xi}{\partial \gamma_{i,1}^{k=6}} \quad (33)$$

By including the chain rule, it is stated as follows in Eq. (34).

$$\Delta \gamma_{i,1}^{k=6} = -\epsilon \frac{\partial \xi}{\partial \gamma_1^k} \times \frac{\partial \gamma_1^k}{\partial \alpha_{1k}} \times \frac{\partial \alpha_{1k}}{\partial \gamma_{i,1}^{k=6}} \quad (34)$$

It is feasible to acquire the weight value adjusted as given in Eq. 35 by applying the chain rule (substituting Eq. (34)).

$$\Delta \gamma_{i,1k=6} = \epsilon (T \arg et_1 - \gamma_1^k) \times \gamma_{1k} (1 - \gamma_{1k}) \times (\gamma_i^k), \Delta \gamma_{i,1}^k \epsilon \mu_{1k} \gamma_i^k, \quad (35)$$

where, $\mu_{1k} = (T \arg et_1 - \gamma_{1k}) \times \gamma_{1k} (1 - \gamma_{1k})$, and so on.

$$\begin{aligned} \Delta \beta_{j,i^k} \alpha - \left[\sum_l \frac{\partial \xi}{\partial \gamma_{jk}} \times \frac{\partial \gamma_{jk}}{\partial \alpha_{jk}} \times \frac{\partial \alpha_{jk}}{\partial \gamma_{jk}} \right] \times \frac{\partial \gamma_{jk}}{\partial \alpha_{jk}} \times \frac{\partial \alpha_{jk}}{\partial \beta_{j,i^k}} \\ \Delta \beta_{j,i^k} = -\epsilon \left[\sum_l \frac{\partial \xi}{\partial \gamma_{jk}} \times \frac{\partial \gamma_{jk}}{\partial \alpha_{jk}} \times \frac{\partial \alpha_{jk}}{\partial \gamma_{jk}} \right] \times \frac{\partial \gamma_{jk}}{\partial \alpha_{jk}} \times \frac{\partial \alpha_{jk}}{\partial \beta_{j,i^k}} \\ \Delta \beta_{j,i^k} = \epsilon \left[\sum_1 (T \arg et_1 - \gamma_1^k) \times \gamma_{1k} (1 - \gamma_{1k}) \times (\gamma_i^k) \right] \times \gamma_{1k} (1 - \gamma_{1k}) \times \eta_j \\ \Delta \beta_{j,i^k} = \epsilon \left[\sum_1 \mu_{1k} (x_{i,1k}) \right] \times \gamma_{i^k} (1 - \gamma_{i^k}) \times \eta_j \\ \Delta \beta_{j,i^k} = \epsilon \mu_{ik} \eta_j \\ \mu_{i^k} = \left[\sum_1 \mu_{1k} (x_{i,1k}) \right] \times \gamma_{i^k} (1 - \gamma_{i^k}) \end{aligned}$$

The weights in Eq. (36)'s output and hidden layers represent the updates and biases between them:

$$x_{i,1k=6}^+ = x_{i,1k=6} + \delta_{e^{k=6}} \Delta \gamma_{i,1k=6} \quad (36)$$

The weight and bias adjustments between the input and hidden layers are shown in Eq. (37) as follows:

$$\beta_{j,ik}^+ = \beta_{j,ik} + \delta_{e^k} \Delta \beta_{j,ik} \quad (37)$$

where, δ_e represent the learning rate of DELM and the value of δ_e is between 0 and 1.

4 Results and discussion

The analysis is done on the experimental findings related to the suggested fusion-based lung cancer detection method. The suggested model is developed using the MATLAB platform on a machine running Windows 10 with a 6 GB RAM configuration and an Intel Core i5 CPU. Performance measures include precision, accuracy, sensitivity, recall, F-measure, specificity, NPV (Negative Predictive Value), MCC (Mathew's Correlation Coefficient), FRR, FPR (False Positive Rate), and FNR (False Negative Rate) are used to compare and evaluate the suggested work (False Rejection Rate).

4.1 Dataset description

For experimental analysis, MRI and PET lung images are used. These images are gathered from Aarthi Scans and Labs and CT Scan Centers in Nagercoil. In this, 500 lung cancer patient images are collected for classification process. Among the images, 80% images are used for training and 20% images are used for testing.

4.2 Experimental results

The experimental findings from the suggested lung disease categorization are provided in this section. Performance is compared with that of various classifiers, including those that classify lung cancer using deep neural networks (DNN), artificial neural networks (ANN),

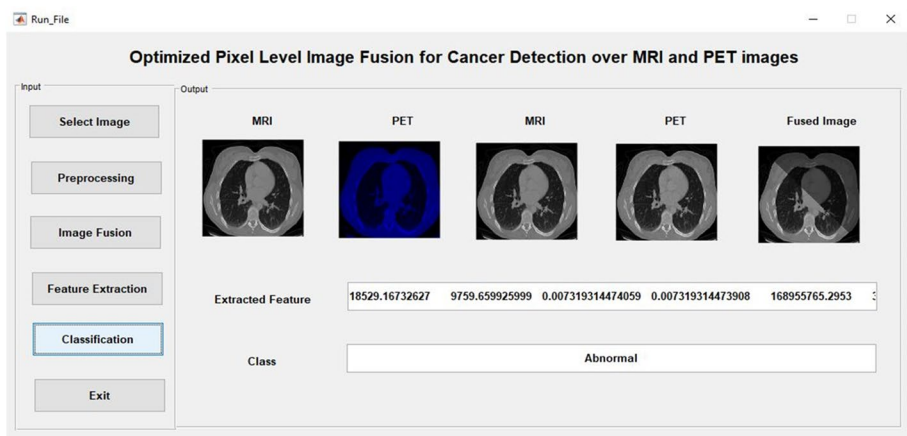


Fig. 8 Screenshot for abnormal class

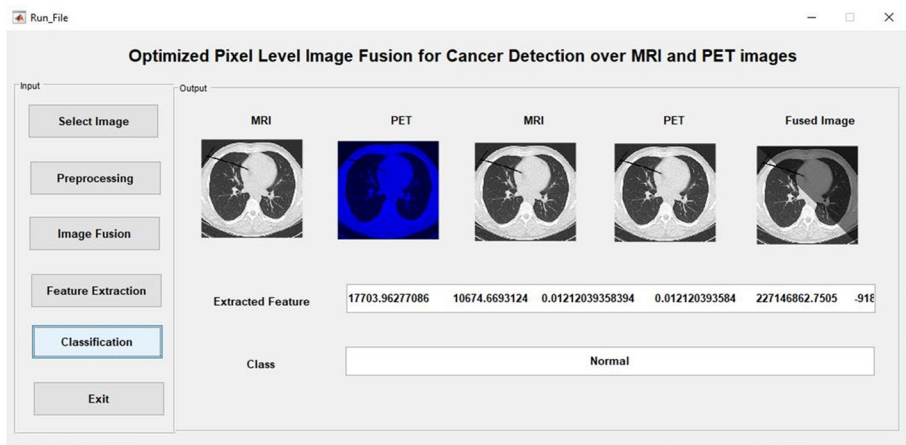

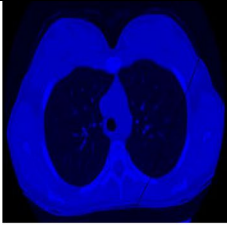

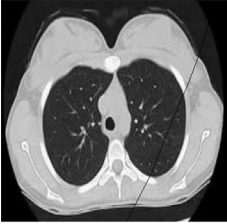
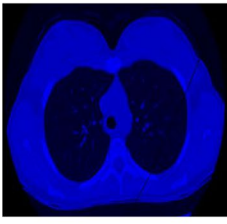

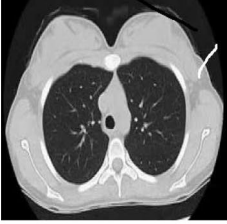
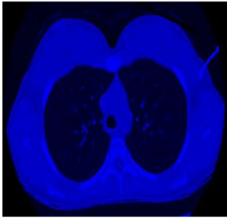


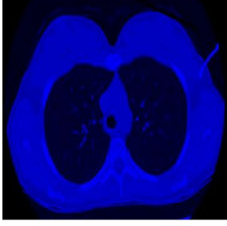


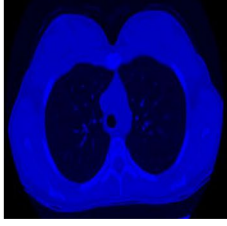



Fig. 9 Screenshot for normal class

convolution neural networks (CNN), and support vector machines (SVM), to confirm the effectiveness of the planned strategy. It shows the Screenshot for abnormal class and Screenshot for normal class in Figs. 8 and 9. The output image of fusion is given in Tables 1 and 2.

In Fig. 10, sensitivity, specificity, accuracy, as well as existing and proposed classifier performance are analyzed. The proposed DELM has a sensitivity difference of 0.019, 0.0857, 0.1428, and 0.1809 respectively over DNN, CNN, ANN, and SVM. Compared to other existing classifiers, the DELM achieved the highest specificity of 0.9655. Similar to DNN, CNN, ANN, and SVM, DELM accuracy differs by 0.019, 0.0857, 0.1428, and 0.1809 respectively. The proposed DELM exhibits greater performance based on all these contrasted values. Figure 11 compares the proposed and current classifiers' performances in terms of metrics like recall, accuracy, and F-measure. The suggested DELM's F-measure outperforms the DNN, CNN, ANN, and SVM, respectively, by 0.02, 0.0948, 0.1546, and 0.1862. When a recall is taken into account, the proposed DELM performs better since the current ANN and SVM perform worse than the existing CNN, DNN, and the proposed BELM. Additionally, the suggested DELM shows greater performance in terms of accuracy. As a result, it can be concluded that the strategy that is suggested performs better than the compared measures. Figure 12 compares the suggested performance to that of the classifiers that are currently in use for measures like NPV and MCC. The existing SVM has relatively poor performance about MCC, as indicated by the result of 0.5468, which is low when compared to the other specified classifiers. When compared to the current ANN and SVM, the DNN and CNN are superior. But the suggested DELM performs better when compared to all of those widely used methods. Both the planned DELM and the DNN's NPV, which are 0.9473 and 0.9491, respectively, are roughly close. However, the suggested DELM performs better than any other classifiers. Additionally, utilizing metrics like FPR and FNR, Fig. 13 contrasts the performance of the proposed classifier with that of the existing classifiers. From Fig. 4, it can be deduced that the SVM performs the least well among all classifiers, having the largest FPR and FNR. The performance of the current SVM is judged to be the worst out of all the compared classifiers. The findings section explains that the performance of the existing classifiers, SVM and ANN, is much worse than that of the other classifiers. The suggested DELM performs better than the current CNN and DNN classifiers, which are superior when compared to SVM and ANN.

Table 1 Image fusion output

MRI image	PET image	Fused image
		
		
		
		
		

4.3 Comparison with the published paper

We contrast our results with many published articles to confirm the viability of the suggested methodology. Due to this, we carried out a series of trials using four newly

Table 2 Overall output

Methods	Sen	Spec	Accur	Precision	Recall	F-Measure	NPV	FPR	FNR	MCC
Proposed ATSO + DELM	0.936	0.965	0.97	0.966	0.936	0.946	0.949	0.034	0.063	0.903
DNN	0.936	0.931	0.933	0.916	0.936	0.926	0.947	0.068	0.063	0.865
CNN	0.872	0.862	0.866	0.836	0.872	0.854	0.892	0.137	0.127	0.731
ANN	0.808	0.810	0.809	0.775	0.808	0.791	0.839	0.189	0.191	0.616
SVM	0.808	0.741	0.771	0.716	0.808	0.76	0.826	0.258	0.191	0.546

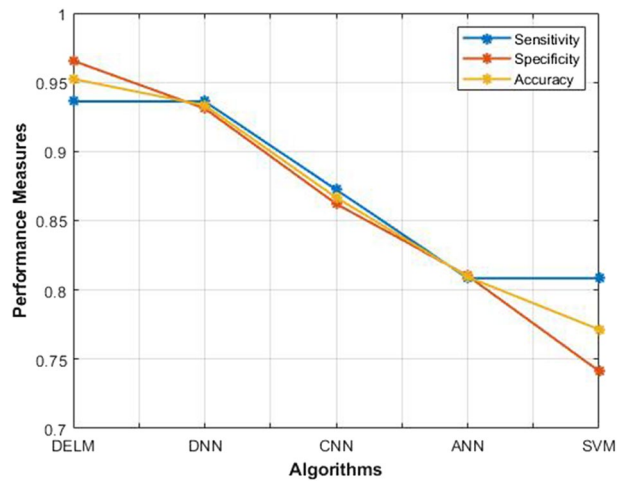
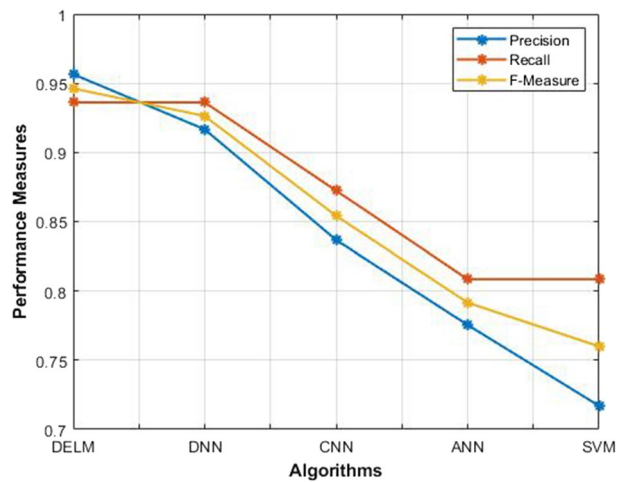
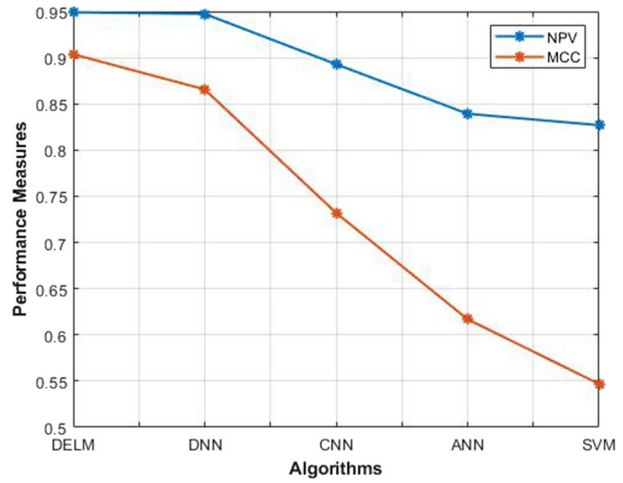
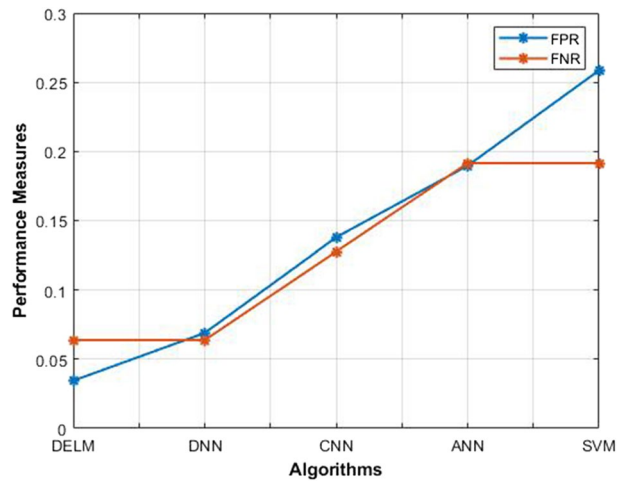
Fig. 10 Performance analysis of accuracy, sensitivity and specificity**Fig. 11** Performance analysis of recall precision and F-measure

Fig. 12 Performance analysis of MCC and NPV**Fig. 13** Performance analysis of FPR and FNR**Table 3** Comparative outcomes

Reference	Methods	Accuracy	Sensitivity	Specificity
[10]	FPSO + CNN	90.85	-	-
[11]	DGMM-RBCNN	0.8779	0.70	0.91
[12]	CNN	95.96	95.3	-
[13]	Neuro fuzzy classifier	89.96	89.6	80.87
Proposed	ATSO + DELM	0.9723	0.9461	0.9655

published approaches for classifying lung cancer [10, 11, 12, and 13]. Table 3 presents the comparative outcomes.

When analyzing Table 2, we understand that our proposed method attained the maximum accuracy, sensitivity, and specificity. This is due to DELM and the fusion technique. State-of-the-art techniques focus only on classification. Our research focuses on fusion before classification to improve classification accuracy. It gives better classification results.

5 Conclusion

An efficient automatic lung disease classification using the DELM technique has been presented in this study. To achieve this objective, image fusion has played a major role in this paper. Because fusing the medical images significantly took part in helping doctors effectively diagnose and treat. The proposed lung disease classification has the following stages namely, image fusion, feature extraction, and followed by DELM-based classification. For fusion MRI and PET image has been used. The optimal pixel-level fusion technique has been applied to combine the PET and MRI images. Here, to enhance the fusion model, the fusion parameter present in the technique has been optimally selected using the ATSO algorithm. For classification, the DELM technique has been presented which effectively overcomes the difficulties present in the ELM and DNN. The presented method achieved a maximum accuracy of 97.23%. As an extension of the proposed model, it can be enhanced through the development of an adaptive model and severity analysis for additional multiple-class datasets (more than 5). Besides, we will try to apply this technique to other disease detection.

Authors' contributions All authors read and approved the final manuscript.

Funding The authors declare that they have competing interests and funding.

Data availability Data sharing not applicable to this article as no datasets were generated or analysed during the current study.

Code availability Code is available.

Declarations

Conflict of interests On behalf of all authors, the corresponding author states that there is no conflict of interest.

References

1. Cassim S, Kidd J, Rolleston A, Keenan R, Aitken D, Firth M, Middleton K, Chepulis L, Wong J, Hokowhitu B, Lawrenson R (2021) Hā Ora: Barriers and enablers to early diagnosis of lung cancer in primary healthcare for Māori communities. *Eur J Cancer Care* 30(2):e13380
2. MacLean A, Hunt K, Smith S, Wyke S (2017) Does gender matter? An analysis of men's and women's accounts of responding to symptoms of lung cancer. *Soc Sci Med* 191:134–142
3. Wielpütz M, Kauczor HU (2012) MRI of the lung: state of the art. *Diagn Interv Radiol* 18(4):344–353
4. Mansoor A, Bagci U, Foster B, Xu Z, Papadakis GZ, Folio LR, Udupa JK, Mollura DJ (2015) Segmentation and image analysis of abnormal lungs at CT: current approaches, challenges, and future trends. *Radiographics* 35(4):1056

5. Kaur H, Koundal D, Kadyan V (2021) Image fusion techniques: a survey. *Arch Computational Methods Eng* 28(7):4425–4447
6. Li S, Kang X, Fang L, Hu J, Yin H (2017) Pixel-level image fusion: A survey of the state of the art. *Information Fusion* 33:100–112. <https://doi.org/10.1016/j.inffus.2016.05.004>
7. Razzak, MI, Naz, S, Zaib, A (2018) Deep learning for medical image processing: Overview, challenges and the future. *Classification in BioApps*, pp.323–350. https://doi.org/10.1007/978-3-319-65981-7_12
8. Kiran MS (2015) TSA: Tree-seed algorithm for continuous optimization. *Expert Syst Appl* 42(19):6686–6698
9. Uzair M, Shafait F, Ghanem B, Mian A (2018) Representation learning with deep extreme learning machines for efficient image set classification. *Neural Comput Appl* 30(4):1211–1223
10. Asuntha A, Srinivasan A (2020) Deep learning for lung Cancer detection and classification. *Multimed Tools Appl* 79(11):7731–7762
11. Jena SR, George ST, Ponraj DN (2021) Lung cancer detection and classification with DGMM-RBCNN technique. *Neural Comput Appl* 33(22):15601–15617
12. Guo Z, Xu L, Si Y, Razmjoooy N (2021) Novel computer-aided lung cancer detection based on convolutional neural network-based and feature-based classifiers using metaheuristics. *Int J Imaging Syst Technol* 31(4):1954–1969
13. Akter O, Moni MA, Islam MM, Quinn JM, Kamal AHM (2021) Lung cancer detection using enhanced segmentation accuracy. *Appl Intell* 51(6):3391–3404
14. Parvathy VS, Pothiraj S (2020) Multi-modality medical image fusion using hybridization of binary crow search optimization. *Health Care Manag Sci* 23(4):661–669
15. Wang Z, Li X, Duan H, Su Y, Zhang X, Guan X (2021) Medical image fusion based on convolutional neural networks and non-subsampled contourlet transform. *Expert Syst Appl* 171:114574
16. Fu J, Li W, Ouyang A, He B (2021) Multimodal biomedical image fusion method via rolling guidance filter and deep convolutional neural networks. *Optik* 237:166726
17. Lewis J, O'Callaghan R, Nikolov S, Bull D, Canagarajah N (2007) Pixel- and region based image fusion with complex wavelets. *Information Fusion* 8(2):119–130
18. Petrovic VS, Xydeas CS (2004) Gradient-based multiresolution image fusion. *IEEE Trans Image Process* 13(2):228–237

Publisher's Note Springer Nature remains neutral with regard to jurisdictional claims in published maps and institutional affiliations.

Springer Nature or its licensor (e.g. a society or other partner) holds exclusive rights to this article under a publishing agreement with the author(s) or other rightsholder(s); author self-archiving of the accepted manuscript version of this article is solely governed by the terms of such publishing agreement and applicable law.